3D X-Ray Nanotomography of Cells Grown on Electrospun Scaffolds

Robert S. Bradley, Ian K. Robinson, Mohammed Yusuf*

Here, it is demonstrated that X-ray nanotomography with Zernike phase contrast can be used for 3D imaging of cells grown on electrospun polymer scaffolds. The scaffold fibers and cells are simultaneously imaged, enabling the influence of scaffold architecture on cell location and morphology to be studied. The high resolution enables subcellular details to be revealed. The X-ray imaging conditions were optimized to reduce scan times, making it feasible to scan multiple regions of interest in relatively large samples. An image processing procedure is presented which enables scaffold characteristics and cell location to be quantified. The procedure is demonstrated by comparing the ingrowth of cells after culture for 3 and 6 days.

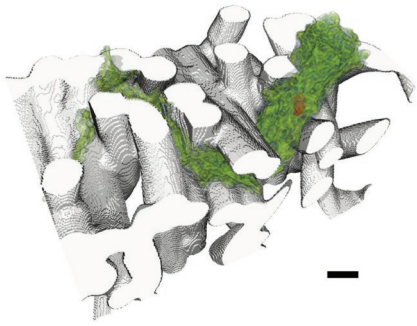

1. Introduction

Tissue engineering aims to recover the function of damaged tissues and organs by combining techniques from life sciences and engineering. A key strategy is to develop implantable 3D scaffolds onto which cells are seeded and grown. The scaffolds must provide analogous functions to that of the extracellular matrix of the target tissue, which is achieved by designing a structure with suitable architecture, mechanical properties, cytocompatibility, and bioactivity.[1] Scaffold architecture is important in achieving good cell adhesion and hence high cell seeding efficiencies, with porosity and surface area to volume ratio being key characteristics.[2,3] Pore space diameter and pore connectivity are important for tissue-ingrowth and vascularization.[3]

Imaging plays an important role in assessing these characteristics and in the understanding of the growth of cells in scaffolds. 3D quantitative information can be obtained on scaffold architecture, including how it changes over time, and on cell infiltration and differentiation. Appel et al.[4] reviewed 3D imaging approaches for tissue engineering applications and highlighted the need for further technique development to address all imaging requirements. State-of-the-art optical imaging techniques, such as multiphoton laser confocal fluorescence microscopy (LSCM) and light sheet microscopy, are being increasingly used and can provide 3D information at spatial resolutions down to ≈0.2 μm for relatively thick but translucent specimens.[5] The information revealed however is sparse, in that only fluorescently labelled structures are imaged,

Dr. R. S. Bradley[+]
Henry Moseley X-ray Imaging Facility
The University of Manchester
Oxford Road, Manchester M13 9PL, UK
Prof. I. K. Robinson, Dr. M. Yusuf
London Centre for Nanotechnology
University College London
Gower Street, London WC1E 6BT, UK
E-mail: yusuf.mohammed@ucl.ac.uk
Prof. I. K. Robinson, Dr. M. Yusuf
Research Complex at Harwell
Rutherford Appleton Laboratory
Didcot OX11 0FA, UK
[+]Present address: Geotek Ltd, 4 Sopwith Way, Daventry NN11 8PB, UK

while the spatial resolution is typically not isotropic and the signal-to-noise ratio decreases with depth. Furthermore, high light intensities are often required which can lead to fluorophore bleaching and phototoxic effects.[5] At higher resolution, destructive imaging techniques such as FIB-SEM can be used, which are particularly suited to analyzing cell interactions with nanostructured scaffolds.[6–8] However FIB-SEM has a limited field of view and is suited to imaging near surface features.

High-resolution X-ray tomography is a promising alternative for nondestructive 3D imaging at resolutions from tens of microns to tens of nanometers.[9] X-ray absorption provides excellent contrast for hard tissues and microCT is being widely adopted for studying osteogenesis in bone constructs.[10–12] However, at hard X-ray energies, absorption contrast is poor for soft tissues and light materials such as polymer scaffolds. Contrast is much greater at soft X-ray energies in the water window (284–543 eV) with resolutions down to ≈10 nm being achieved by soft X-ray microscopes.[9] However, X-ray penetration is only ≈15 μm for cells, limiting the applicability of the technique for studying 3D tissue engineering constructs. Contrast agents can be used to improve X-ray absorption at higher X-ray energies. For example, phosphotungstic acid and iodine based stains have been used to visualize and characterize in-vitro engineered extracellular matrix,[13] while osmium tetroxide has been used to stain cells seeded on polymer scaffolds.[14,15] Zehbe et al.[16] used a combined Au/Ag stain to image chondrocytes seeded on gelatine scaffolds, while Thimm et al.[17] used targeted FeO particles to label endothelial cells in polyurethane scaffolds. However, it may be difficult to achieve uniform staining across a sample (particularly for small pore scaffolds)[16,18] and nonspecific staining can reduce sensitivity. For example, Dorsey et al.[14] concluded that microCT was five times less sensitive for detecting cells than a DNA assay and is hence limited to quantifying cell densities greater than a million cells mL^{-1}.

Phase contrast imaging techniques can overcome these limitations by generating contrast from the real part of the object's refractive index, which can be 1000 times greater at hard X-ray energies than the real part which gives rise to absorption.[9] There is a variety of X-ray phase imaging techniques being actively developed. At the micron resolution scale, phase contrast imaging has been used to visualize the microstructure of polymer and gelatine scaffolds[19–21] as well as their degradation after implantation.[22] Zehbe et al.[23] demonstrated that cellular level detail can be obtained yielding comparable information to conventional histology for articular cartilage tissue. Recently, Hagen et al.[24] compared different phase contrast techniques for imaging the microstructure of decelluarlized tissues. At higher resolutions, Zernike phase contrast and coherent diffraction imaging have been used to image single cells or clusters of cells with subcellular detail.[25–28]

In this paper, we demonstrate that laboratory X-ray phase contrast nanotomography can be used to image cells, with subcellular detail, seeded on polymer scaffolds while also providing key information on both cell location and scaffold architecture. The linking together of 3D information on both cells and scaffolds has the potential to provide new insights into cytocompatibility and bioactivity. The X-ray imaging conditions were optimized to enable lower dose, higher throughput region-of-interest (ROI) scanning of relatively large specimens. An image processing procedure has been developed to enable scaffold characteristics and cell location to be quantified. The procedure is demonstrated by comparing cell infiltration into polymer scaffolds after culture for 3 and 6 days.

2. Experimental Section

2.1. Sample Preparation

Samples were prepared using the protocols described in refs.[29,30]. Briefly, electrospun poly(lactide-*co*-glycolide) (PLGA) scaffolds in the form of disks of diameter ≈2 cm and thickness of ≈70 μm, with fiber diameter of ≈4 μm, were purchased from the Electrospinning Company, UK. Cell culture using human fibroblast cells was carried out for 3 and 6 days. Scaffolds containing cells were then fixed using 2.5% (vol/vol) glutaraldehyde in 0.1 M cacodylate buffer (pH 7.2) for 2 h. Samples were then washed three times with 0.1 M cacodylate buffer (pH 7.2), dehydrated using a series of ethanol solutions (70%, 85%, and 100%), and finally dried using hexamethyldisilazane (Sigma-Aldrich, UK) for 5 min.

2.2. X-Ray Nanotomography

Strips of the scaffolds of ≈200–500 μm in width were prepared mechanically and placed within 1 mm diameter kapton tubing for X-ray scanning. The samples were scanned using a Zeiss Xradia Ultra-810 system using the 150 nm resolution optics with Zernike phase contrast.[31] The system is a zone plate transmission X-ray microscope with a 65 μm field of view and uses quasimonochromatic X-rays with energy of 5.4 keV. A schematic diagram of the system is shown is Figure 1. The scaffolds were however found to be sensitive to high X-ray dose, with long scans (≈8 h) leading with damage of the fibers, as manifested as large holes appearing in the scaffold. The scan settings were therefore optimized to reduce dose while maintaining an acceptable contrast to noise ratio. The exposure time was set to 10 s per radiograph and 541 radiographs were taken over 180°, giving a scan time of ≈1 h 37 min. Volumetric data were reconstructed with a voxel size of 127 nm using filtered-back projection, using the ASTRA toolbox[32] via the TomoTools interface.[33]

Macromol. Biosci. **2017**, DOI: 10.1002/mabi.201600236

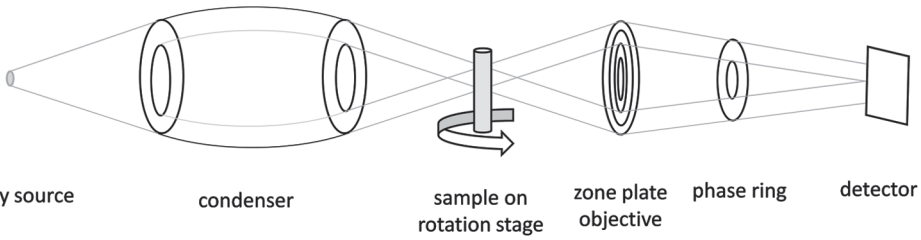

Figure 1. Schematic diagram of a transmission X-ray microscope with Zernike phase contrast. The X-ray paths are shown in gray and phase contrast is achieved via the phase ring placed in the back focal plane of the zone plate objective.

Two overlapping scans were taken at each ROI to image the full thickness of the scaffold and the volumetric data stitched together after reconstruction. Further details are given in the image analysis section.

Scans were taken at 3 ROIs for 2 scaffold sections prepared from the same sample at each time point, giving six ROIs in total for each of the 3 and 6 day time points. The total scaffold volume sampled per time point was $\approx 2.5 \times 10^6$ μm^3.

2.3. Image Analysis

A semiautomatic image processing procedure was developed to aid visualization and enable quantification of scaffold architecture as well as the infiltration of the cells into the scaffolds. The procedure comprised the following six stages.

2.3.1. Stitching of Data Sets

The two overlapping scans per ROI were stitched together by first aligning the data automatically using the image processing toolbox in Matlab 2014a (Mathworks, Natick, MA). The gray levels of the two volumes in the overlap region were matched prior to stitching by finding the linear transform of the data in one scan which led to the best agreement between the gray level cumulative density functions. The data from the two scans in the overlap region were then averaged, as shown in Figure 2a.

2.3.2. Removal of the Phase Contrast Artifacts

The Zernike method of phase contrast imaging typically gives rise to halo artifacts at the edges of features.[31] While these artifacts aid feature detection, they can make segmentation more difficult. Therefore, an image filter was developed to remove the phase contrast artifacts inspired by the model of Zernike phase contrast for optical microscopes by Yin et al.[34] In this model the artifacts in the 2D optical images were given by a convolution kernel applied to artifact-free images, where the kernel involved an obscured Airy function (difference between Bessel's functions). We propose the following simpler 3D convolution kernel which gives rise to the artifacts in the tomographic reconstructed slices

$$F(\mathbf{r}) = A\delta(\mathbf{r}) + B\mathrm{DoG}(\mathbf{r},\sigma_1,\sigma_2) \quad (1)$$

where $\mathbf{r}$ is position, δ is the delta function and DoG is the difference between two 3D Gaussians with mean zero and isotropic standard deviations, σ_1 and σ_2. Deconvolution with the above kernel then gives volumetric data with the artifacts removed or reduced. Total variation regularization was used for the deconvolution, via the approach of Chan et al.,[35] in order to reduce the effects of noise.

Suitable values of the standard deviations (σ_1 and σ_2) and constants (A and B) were obtained via an optimization approach. An ROI containing a single scaffold fiber was selected and the fiber segmented. The segmentation was convolved with the proposed filter (which was evaluated on a $7 \times 7 \times 7$ grid) to simulate data with Zernike artifacts. The parameters were then optimized so that the simulated artifact data was in good agreement (in terms of least squared difference) with the acquired tomographic data for that ROI.

For the total variation (TV) deconvolution, the amount of regularization was controlled by a single parameter, whose values was chosen as a compromise between artifact removal and noise propagation, and was kept constant for all data sets. Examples of reconstructed slices before and after artifact reduction are shown in Figure 2.

2.3.3. Segmentation of the Scaffold Fibers

Segmentation of the fibers was based on identifying structures with a local thickness similar in value to the known fiber diameter of ≈4 μm. First a gray level threshold was applied to segment both cells and fibers, with opening and closing morphological operations applied to remove small islands. The 3D local thickness was then calculated using ImageJ[36] and hysteresis thresholding was applied to the thickness data to preferentially select the fibers. An example slice through the local thickness data is given in Figure 3a. Manual adjustment was carried out as necessary to remove any remaining regions corresponding to cells or background.

2.3.4. Segmentation of the Cells

Region growing was used to segment the cells in the regions identified in step 3 as not corresponding to fibers. Low frequency variations in greyscale across the volume (particularly towards the edges of the field of view), arising from the deconvolution in step 2, meant that 3D region growing with a single greyscale threshold could not be used. Instead, 2D region growing was applied slice by slice with the threshold being manually adapted. For quantification of cell infiltration, this procedure was carried out on every 10th slice in order to reduce processing time.

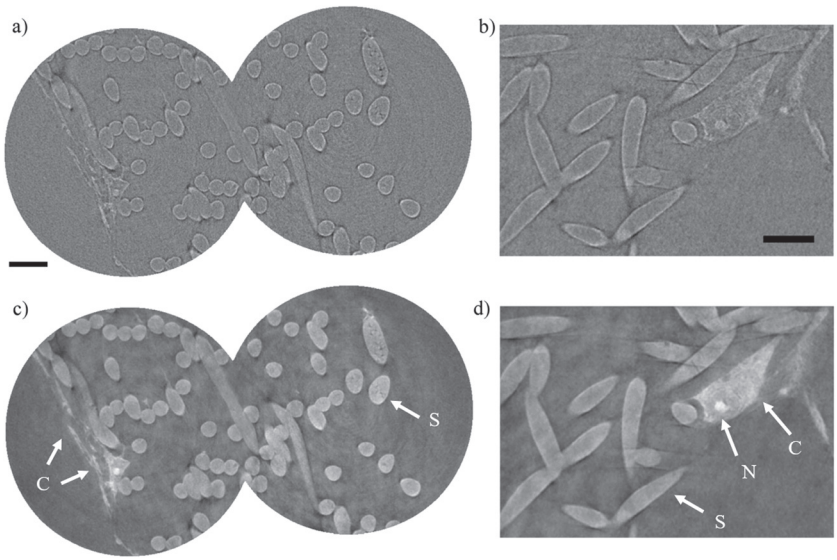

Figure 2. a) Reconstructed slice through a scaffold after stitching together 2 scans. The upper scaffold surface is on the left-hand side. Scale bar is 15 μm. b) Enlarged section of a slice showing a cell with subcellular detail clearly visible. Scale bar is 15 μm. The corresponding slices after phase artifact removal are shown in panels (c) and (d). S, scaffold; C, cell; N, nucleus.

2.3.5. Quantifying the Distance of Cells from the Upper Scaffold Surface

The upper surface of the scaffold (the surface on which cells were seeded) was determined by fitting a 2D plane to the upper most voxels of the fiber segmentation. The volumetric data were split into a 5×5 grid along the two axes that were approximately parallel to the scaffold surface, and the fiber voxel in each grid with the minimum z coordinate (along the scaffold depth direction) was identified. A plane was then fitted to the coordinates of these 25 voxels using the RANSAC algorithm, using the Matlab code available from http://www.peterkovesi.com/matlabfns/index.html. An example of a fitted plane is given in Figure 3b. The depth of each cell voxel was then calculated as the perpendicular distance away from the upper plane. The same procedure was adapted to find the lower scaffold surface and the mean distance between planes was used as a measure of scaffold thickness.

However, the number of voxels, $N(d)$, sampled as a function of distance, d, from the scaffold surface is nonuniform as the stitched data comprises two overlapping cylinders (see Figure 2). Therefore, when calculating the histograms of cell volume as a function of distance, the distribution for each ROI was weighted by $N_{max}/N(d)$, where N_{max} is the maximum value of N over all d and all ROIs. This weighting also accounts for any differences between the total volume scanned for the 3 day and 6 day time points.

2.3.6. Quantifying Scaffold and Cell Characteristics

Scaffold architecture was characterized in terms of porosity, pore size and fiber diameter from sub-regions within each ROI. Pore size was determined using the local thickness measure,[37] while fiber diameter was determined by first skeletonizing the fiber segmentation, using the autoskeleton module in Avizo 9 (FEI VSG, Burlington, MA), and then calculating the modal diameter measure given in.[38] The modal diameter is calculated for every point on the skeleton as the diameter about the skeleton position, and in a plane perpendicular to the local skeleton direction, at which the number of edge voxels is maximized.

The length and diameter of selected cells was measured after first calculating the skeleton, using the autoskeleton module in Avizo 9 (FEI VSG, Burlington, MA), and then applying the post-processing techniques described in.[38] The longest-shorted path between skeleton nodes was used to determine cell length, with the length of this path calculated using the multi-seed sphere-network technique.[38] The cell diameter was calculated on planes perpendicular to this path using the modal diameter measure as described above.

3. Results and Discussion

The reconstructed slices in Figure 2 show that X-ray nanotomography with Zernike phase contrast can reveal both cell morphology and scaffold structure. Subcellular detail is visible even in these short (≈1 h 37 min) scans, in which dose was reduced to avoid the damage occurring to fibers as found for longer scans times (≈8 h). The total dose was estimated to be ≈400 kGy (in the case of complete infiltration of the scaffolds by cells and taking the optical properties of cells to be equal to that of soft tissue). The stitching together of two scans allows the full thickness of the scaffolds to be imaged at 150 nm resolution. However, Zernike phase contrast gives rise to halo artifacts around features, which makes image segmentation more difficult. These artifacts arise from diffracted X-rays from the sample, having low angular deviation, passing through the phase ring.[39] These artifacts were almost all removed by deconvolution with the image filter given in Equation (1), while making use of this signal (and hence the low angular deviation diffracted X-rays) to increase contrast across features (not just at edges). Examples of reconstructed slices before and after phase artifact reduction are shown in Figure 2a–d. Recently, Kumar et al.[40] developed a full model of Zernike phase contrast for Fresnel zone plate X-ray microscopes, allowing the Zernike artifacts to be removed by a similar deconvolution approach. However their model is complex to implement, and regularization for the deconvolution step requires eight user-defined parameters to be optimized. In comparison, the approach developed in this paper is simpler and more practical,

Macromol. Biosci. **2017**, DOI: 10.1002/mabi.201600236

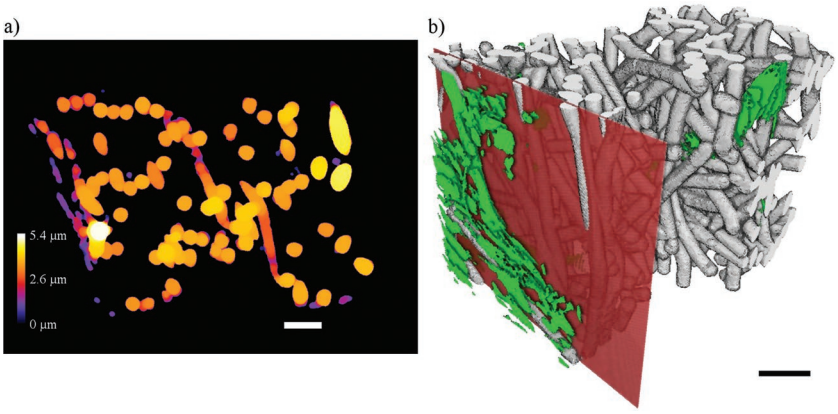

Figure 3. a) Local thickness map used in step 3 of the segmentation process (see Section 2.3) shown for the slice in Figure 2a. Scale bar is 10 µm. b) 3D rendering of the segmented data with fibers in gray and cells in green. The 2D plane fitted to the upper scaffold surface is shown in red. Scale bar is 20 µm.

requiring only one parameter to be optimized. Some loss of resolution is however evident (and hence loss of some subcellular detail, see figure 2), with the estimated resolution (from line profiles taken perpendicular to the fiber edges) being ≈320 nm, corresponding to ≈2.5 x the voxel size.

The grayscales of scaffold and cells are similar although subcellular features (i.e., the nucleus/nucleolus) do show a clear enhancement. To understand this, the real part of the refractive index (giving rise to the phase contrast) was estimated for PLGA to be $\approx 9.4 \times 10^{-6}$ (using tabulated optical constants from http://henke.lbl.gov/optical_constants/). For comparison, the value for cytoplasm was calculated from the measured electron density of frozen hydrated cells[28] to be similar at 8.2×10^{-6}, while that of organelles was estimated to be higher at 1×10^{-5}. The sample preparation technique used in this study can lead to cell shrinkage,[41] and hence an increase in the real part of the refractive index in comparison to frozen hydrated cells. This would give rise to similar overall contrast for scaffold and cells at the current imaging resolution, as observed, while increasing the contrast of clearly resolved organelles. However, it should be noted that the greyscales are not a direct quantitative measure of phase shift produced by the sample, in part because the Zernike technique gives rise to a mixture of absorption and phase contrast (and is only proportional to phase shift in the weakly absorbing case when the phase shift is relatively small or slowly varying[39]), and because the artifact removal algorithm lacks a rigorous theoretical underpinning.

Segmentation of the cells and fibers facilitates 3D visualization of the data as well as quantitative analysis. A 3D rendering of a scaffold with cells grown for 3 d is given in Figure 4, showing that the majority of the cells are at or close to the upper scaffold surface. Subcellular detail is clearly visible, including the nucleus (see also Figures 2 and 5) and a texture which may be associated with the cytoskeleton and other organelles. The interplay between cell morphology and fiber arrangement is shown in greater detail in Figure 5 for a single cell at a depth of ≈43 µm after culture for 6 d. The fiber arrangement has constricted the growth of the cell such that it takes a tortuous path between fibers, with the cell length being 41.5 µm in comparison to the Euclidean distance across the cell (from skeleton path start and end points, see Section 2.3) being 24.9 µm. The diameter of the cell has also been restricted, with the modal diameter taking values in the range 0.6 to 3.2 µm, with the median value being 1.6 µm.

Surface imaging of cells grown in electrospun scaffolds using SEM has previously been reported.[29] In this study we show that cell migration has occurred across the full thicknesses of the scaffolds, with the thicknesses measured to be in the range 68 to 88 µm. The distribution of cell volume with distance is shown for a single ROI in Figure 6 and overall ROIs in Figure 7. The shape of the histogram is essentially unaffected by segmenting the cells on every 10th slice in comparison to a full segmentation, as shown in Figure 6.

The overall distributions provide evidence for greater migration of the cells into the scaffold after 6 d. For example, the proportion of cell volume at a depth of 40 µm or greater increased on average (over the ROIs) from 3.8% to 8.5% (the weighted proportion increased from 3.6% to 7.7%) between 3 and 6 d. This proportion was

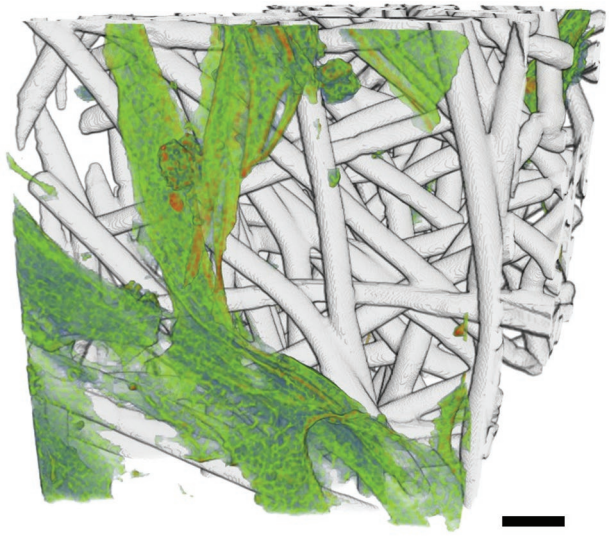

Figure 4. 3D rendering showing cells distributed on and within the scaffold after being grown for 3 d. Subcelluar details are evident, including the nucleus (shown in red) and texture associated with the cytoskeleton and other organelles. Scale bar is 10 µm.

Macromol. Biosci. **2017**, DOI: 10.1002/mabi.201600236

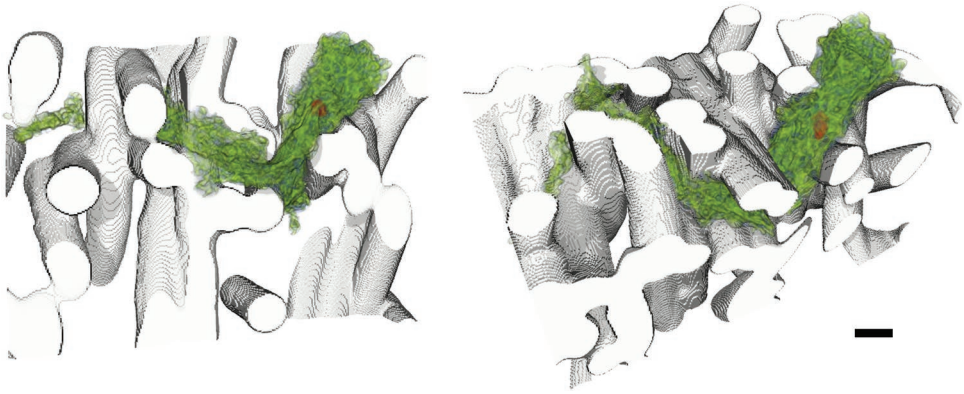

Figure 5. 3D renderings of a cell located at ≈43 μm into a scaffold after culturing for 6 d. The cell morphology is clearly influenced by the local distribution of fibers and their orientation. The cell nucleus is shown in red. Scale bar is 3 μm.

significantly greater for 6 d in 69% of pairwise comparisons (p-value = 0.024 for unweighted and p-value = 0.0001 for weighted volumes) between ROIs at the two time points. There is also evident of an increase in cell volume (averaged over the ROIs) by 42% (two sample t-test, p-value = 0.095), or 53% (p-value = 0.095) for the weighted volume, between 3 and 6 d. The scaffold architecture was very similar for the ROIs at the two times points, including the porosity (77 ± 5% for 3 d and 77 ± 3% for 6 d), the pore space diameter (see Figure 8) and the average fiber diameter, which was measured to be 3.8 ± 0.2 μm for both time points. This suggests that the differences in cell volume and distribution are due to culture time.

However the relatively low cell density for these samples means that the results might not be representative of the scaffolds as a whole. The technique is therefore more suitable for analyzing higher cell densities. The analysis volume per ROI could be increased by ≈60% by stitching together radiographs prior to reconstruction (so that each projection has around twice the field of view along the axis perpendicular to the rotation axis) rather than stitching volumes after reconstruction as was the case in this study.

Overall, it is clear that X-ray phase contrast nanotomography has advantages over 3D optical techniques, such as LSCM, as more complete information is obtained (rather than visualization of only labelled structures) and the image resolution and contrast are isotropic across the field of view, which are conducive to quantitative analysis. The main disadvantage is the limited field of view, even when multiple regions are scanned, which makes quantitative analysis of cell infiltration appropriate when cell densities are high. Furthermore, care must be taken to ensure the X-ray dose is kept sufficiently low not to cause damage to fibers. Cryopreservation techniques could be used to mitigate against high doses and enable higher quality data to be obtained. With these precautions, the technique is essentially nondestructive, and hence it can be combined with complimentary imaging techniques, such as microCT or LSCM, in a hierarchical correlative imaging approach to provide information across length scales.[9] In particular X-ray nanotomography could provide a link between optical imaging and much higher resolution destructive SEM imaging techniques, to enable targeted imaging of preselected features.[23,42] Such a

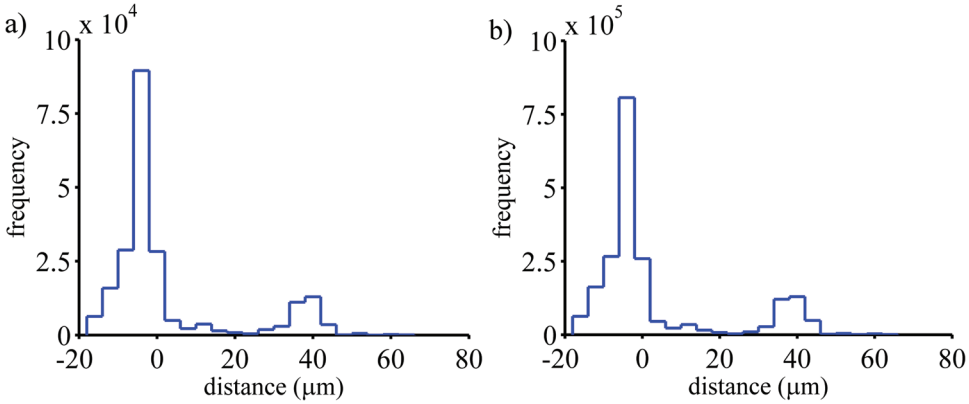

Figure 6. Distribution of the number of cell voxels as a function of distance from the upper scaffold surface for a) segmentation on every 10th slice and b) full cell segmentation for an ROI with cells grown for 3 d.

Macromol. Biosci. **2017**, DOI: 10.1002/mabi.201600236

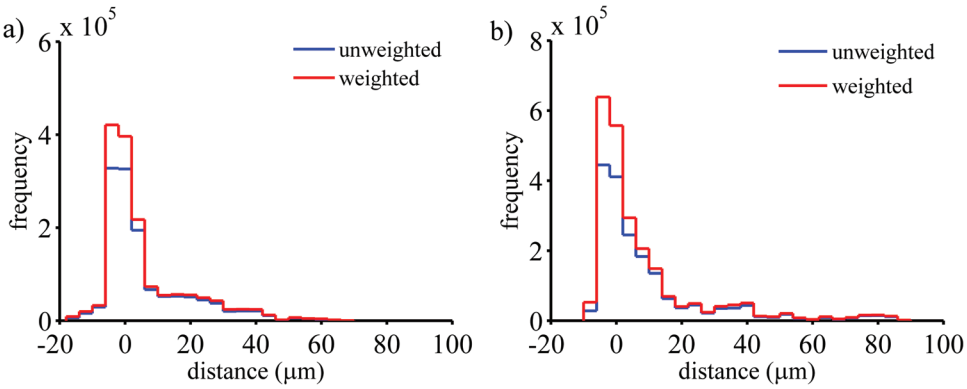

Figure 7. Net distribution over six ROIs of the number of cell voxels as a function of distance from the upper scaffold surface for a) 3 d and b) 6 d. The distributions are shown before and after weighting was applied to account for the nonuniform sampling as a function of distance (see Section 2.3).

correlative imaging approach would allow multiple growth stages to be studied and allow more in-depth information to be gained on the influence of scaffold architecture, for example by varying porosity. 3D imaging of specific cells could be achieved by combining X-ray nanotomography with targeted staining with heavy metals by for example the approach detailed in ref.[16]

4. Conclusions

We have demonstrated that X-ray nanotomography with Zernike phase contrast can be used to image cells in polymer scaffolds at a resolution of 150 nm. The high resolution enables subcellular detail to be obtained while making the technique attractive for characterizing nanofiber scaffolds.[43] The scan settings were optimized to reduce scan times and dose while maintaining an acceptable image quality, making feasible the analysis of multiple regions of interest in relatively large samples. An image processing procedure has been developed to enable quantitative characterization of scaffold architecture as well as determination of cell location and morphology. A proportion of the cells was found to immerse themselves >40 μm deep inside the scaffold and they clearly adhere to the polymer surface. This scaffold material is thereby demonstrated to be a favorable growth environment for the cells. The linking together of 3D information on both cells and scaffold can provide new insights into the interplay between scaffold architecture and cell morphology, cytocompatibility, seeding efficiency, and bioactivity.

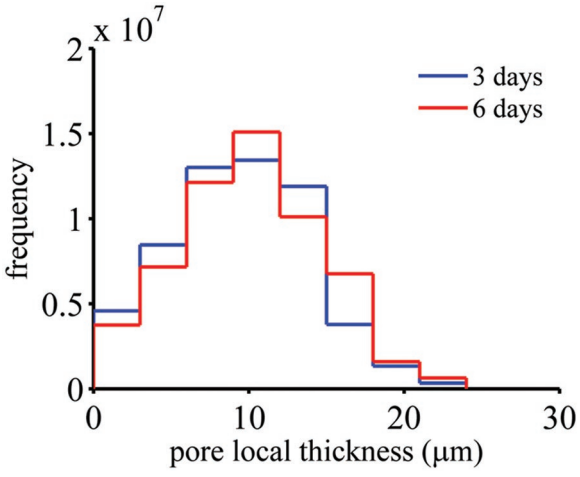

Figure 8. Local thickness distribution of the scaffold pore space for 3 and 6 d over all ROIs. The mean local thickness, averaged over ROIs, is 10.9 ± 4.5 μm and 11.5 ± 4.6 μm for 3 and 6 d, respectively.

Acknowledgements: R.S.B. would like to acknowledge funding via an EPSRC Impact Acceleration Fellowship, EP/M010538/1, and funding for the Henry Moseley X-ray Imaging Facility under EPSRC grants EP/F007906/1, EP/M010619/1 and EP/F028431/1. M.Y. and I.K.R. would like to acknowledge the Biotechnology and Biological Sciences Research Council (BBSRC, UK) through grant BB/H022597/1 and the EPSRC through grant EP/I022562/1. The authors would like to thank the Electrospinning Company, Rutherford Appleton Laboratory, Harwell, Oxford, UK for regular discussion on scaffold material and future directions.

Received: June 9, 2016; Revised: August 9, 2016; Published online: ; DOI: 10.1002/mabi.201600236

Keywords: cell infiltration; electrospun scaffolds; imaging; microstructure; X-ray nanotomography

[1] B. P. Chan, K. W. Leong, *Eur. Spine J.* **2008**, *17*, 467.
[2] M. Costantini, C. Colosi, P. Mozetic, J. Jaroszewicz, A. Tosato, A. Rainer, M. Trombetta, W. Święszkowski, M. Dentini, A. Barbetta, *Mater. Sci. Eng., C* **2016**, *62*, 668.
[3] A. Barbetta, R. Bedini, R. Pecci, M. Dentini, *Ann. Ist. Super. Sanita* **2012**, *48*, 10.

[4] A. A. Appel, M. A. Anastasio, J. C. Larson, E. M. Brey, *Biomaterials* **2013**, *34*, 6615.
[5] F. Pampaloni, E. G. Reynaud, E. H. K. Stelzer, *Nat. Rev. Mol. Cell Biol.* **2007**, *8*, 839.
[6] A. Al-Abboodi, J. Fu, P. M. Doran, P. P. Y. Chan, *Biotechnol. Bioeng.* **2013**, *110*, 318.
[7] E. Lamers, X. F. Walboomers, M. Domanski, G. McKerr, B. M. O'Hagan, C. A. Barnes, L. Peto, R. Luttge, L. A. Winnubst, H. J. Gardeniers, J. A. Jansen, *Tissue Eng., Part C* **2011**, *17*, 1.
[8] R. Wierzbicki, C. Køber, M. R. B. Jensen, J. Łopacińska, M. S. Schmidt, M. Skolimowski, F. Abeille, K. Qvortrup, K. Mølhave, *PLoS One* **2013**, *8*, e53307.
[9] R. S. Bradley, P. J. Withers, *MRS Bull.* **2016**, *41*, 549.
[10] F. Peyrin, *Osteoporosis Int.* **2011**, *22*, 2043.
[11] F. Westhauser, C. Weis, M. Hoellig, T. Swing, G. Schmidmaier, M. A. Weber, W. Stiller, H. U. Kauczor, A. Moghaddam, *R. Soc. Open Sci.* **2015**, *2*, 150496.
[12] X. Wu, L. Wang, F. Deng, D. C. Watts, *Microsc. Res. Tech.* **2014**, *77*, 1037.
[13] I. Papantoniou, M. Sonnaert, L. Geris, F. P. Luyten, J. Schrooten, G. Kerckhofs, *Tissue Eng., Part C* **2014**, *20*, 177.
[14] S. M. Dorsey, S. Lin-Gibson, C. G. Simon Jr, *Biomaterials* **2009**, *30*, 2967.
[15] L. A. Bosworth, S. R. Rathbone, R. S. Bradley, S. H. Cartmell, *J. Mech. Behav. Biomed. Mater.* **2014**, *39*, 175.
[16] R. Zehbe, J. Goebbels, Y. Ibold, U. Gross, H. Schubert, *Acta Biomater.* **2010**, *6*, 2097.
[17] B. W. Thimm, S. Hofmann, P. Schneider, R. Carretta, R. Müller, *Tissue Eng., Part C* **2011**, *18*, 167.
[18] T. Shearer, S. Rawson, S. J. Castro, R. Balint, R. S. Bradley, T. Lowe, J. Vila-Comamala, P. D. Lee, S. H. Cartmell, *Muscles Ligaments Tendons J* **2014**, *4*, 238.
[19] P. Thurner, R. Müller, G. Raeber, U. Sennhauser, J. A. Hubbell, *Microsc. Res. Tech.* **2005**, *66*, 289.
[20] A. Appel, M. A. Anastasio, E. M. Brey, *Tissue Eng., Part B* **2011**, *17*, 321.
[21] R. S. Voronov, S. B. VanGordon, R. L. Shambaugh, D. V. Papavassiliou, V. I. Sikavitsas, *Tissue Eng., Part C* **2012**, *19*, 327.
[22] K. Takashima, M. Hoshino, K. Uesugi, N. Yagi, S. Matsuda, A. Nakahira, N. Osumi, M. Kohzuki, H. Onodera, *J. Synchrotron Radiat.* **2015**, *22*, 136.
[23] R. Zehbe, H. Riesemeier, C. J. Kirkpatrick, C. Brochhausen, *Micron* **2012**, *43*, 1060.
[24] C. K. Hagen, P. Maghsoudlou, G. Totonelli, P. C. Diemoz, M. Endrizzi, L. Rigon, R.-H. Menk, F. Arfelli, D. Dreossi, E. Brun, P. Coan, A. Bravin, P. De Coppi, A. Olivo, *Sci. Rep.* **2015**, *5*, 18156.
[25] M. Stampanoni, R. Mokso, F. Marone, J. Vila-Comamala, S. Gorelick, P. Trtik, K. Jefimovs, C. David, *Phys. Rev. B* **2010**, *81*, 140105.
[26] Y. Yang, W. Li, G. Liu, X. Zhang, J. Chen, W. Wu, Y. Guan, Y. Xiong, Y. Tian, Z. Wu, *J. Microsc.* **2010**, *240*, 14.
[27] R. Mokso, L. Quaroni, F. Marone, S. Irvine, J. Vila-Comamala, A. Blanke, M. Stampanoni, *J. Struct. Biol.* **2012**, *177*, 233.
[28] A. Diaz, B. Malkova, M. Holler, M. Guizar-Sicairos, E. Lima, V. Panneels, G. Pigino, A. G. Bittermann, L. Wettstein, T. Tomizaki, O. Bunk, G. Schertler, T. Ishikawa, R. Wepf, A. Menzel, *J. Struct. Biol.* **2015**, *192*, 461.
[29] M. Yusuf, A. L. G. Millas, A. K. C. Estandarte, G. K. Bhella, R. McKean, E. Bittencourt, I. K. Robinson, *Biotechniques* **2014**, *57*, 137.
[30] A. L. G. Millas, R. McKean, R. Stevens, M. Yusuf, J. V. W. Silveira, M. B. Puzzi, E. Bittencourt, *J. Biomater. Tissue Eng.* **2014**, *4*, 217.
[31] A. Tkachuk, F. Duewer, H. Cui, M. Feser, S. Wang, W. Yun, *Z. Kristallogr.* **2007**, *222*, 650.
[32] W. van Aarle, W. J. Palenstijn, J. De Beenhouwer, T. Altantzis, S. Bals, K. J. Batenburg, J. Sijbers, *Ultramicroscopy* **2015**, *157*, 35.
[33] R. S. Bradley, TomoTools, www.github.com/rsbradley/tomotools (accessed: August **2016**).
[34] Z. Yin, T. Kanade, M. Chen, *Med. Image Anal.* **2012**, *16*, 1047.
[35] S. H. Chan, R. Khoshabeh, K. B. Gibson, P. E. Gill, T. Q. Nguyen, *IEEE Trans. Image Process.* **2011**, *20*, 3097.
[36] R. Dougherty, K.-H. Kunzelmann, *Microsc. Microanal.* **2007**, *13*, 1678.
[37] T. Hildebrand, P. Rüegsegger, *J. Microsc.* **1997**, *185*, 67.
[38] R. S. Bradley, P. J. Withers, *Comput. Biol. Med.* **2016**, *72*, 120.
[39] Y. Yang, R. Heine, Y. Cheng, C.-C. Wang, Y.-F. Song, T. Baumbach, *Appl. Phys. Lett.* **2014**, *105*, 094101.
[40] A. S. Kumar, P. Mandal, Y. Zhang, S. Litster, *J. Appl. Phys.* **2015**, *117*, 183102.
[41] A. Katsen-Globa, N. Puetz, M. M. Gepp, J. C. Neubauer, H. Zimmermann, *Scanning* **2016**.
[42] T. L. Burnett, S. A. McDonald, A. Gholinia, R. Geurts, M. Janus, T. Slater, S. J. Haigh, C. Ornek, F. Almuaili, D. L. Engelberg, G. E. Thompson, P. J. Withers, *Sci. Rep.* **2014**, *4*, 4711.
[43] A. G. Kanani, S. H. Bahrami, *Trends Biomater. Artif. Organs* **2010**, *24*, 93.